

Beating the aliasing limit with aperiodic monotile arrays

Aurelien Mordret^{1,2} and Adolfo G. Grushin³

¹*Department of Geophysics and Sedimentary Basins,
Geological Survey of Denmark and Greenland (GEUS),
Øster Voldgade 10, 1350 Copenhagen K, Denmark**

²*Univ. Grenoble Alpes, Univ. Savoie Mont Blanc, CNRS,
IRD, Univ. Gustave Eiffel, ISTERre, 38000 Grenoble, France*

³*Univ. Grenoble Alpes, CNRS, Grenoble INP, Institut Néel, 38000 Grenoble, France†*

(Dated: August 30, 2024)

Finding optimal wave sampling methods has far-reaching implications in wave physics, such as seismology, acoustics, and telecommunications. A key challenge is surpassing the Whittaker-Nyquist–Shannon (WNS) aliasing limit, establishing a frequency below which the signal cannot be faithfully reconstructed. However, the WNS limit applies only to periodic sampling, opening the door to bypass aliasing by aperiodic sampling. In this work, we investigate the efficiency of a recently discovered family of aperiodic monotile tilings, the Hat family, in overcoming the aliasing limit when spatially sampling a wavefield. By analyzing their spectral properties, we show that monotile aperiodic seismic (MAS) arrays, based on a subset of the Hat tiling family, are efficient in surpassing the WNS sampling limit. Our investigation leads us to propose MAS arrays as a novel design principle for seismic arrays. We show that MAS arrays can outperform regular and other aperiodic arrays in realistic beamforming scenarios using single and distributed sources, including station-position noise. While current seismic arrays optimize beamforming or imaging applications using spiral or regular arrays, MAS arrays can accommodate both, as they share properties with both periodic and aperiodic arrays. More generally, our work suggests that aperiodic monotiles can be an efficient design principle in various fields requiring wave sampling.

I. INTRODUCTION

Sampling – the operation of measuring a continuous analog signal at discrete intervals in time, space, or both – is ubiquitously used in daily life. We find examples in digital audio and video recording and transmission, the Global Positioning System, and health monitoring devices, among many others. It is also an essential component of scientific research, from mathematics and physics to biology, medicine, and Earth science [e.g., 1–3]. Sampling relies on a similar mathematical description across different fields. For example, the problem of sampling seismic waves using a seismic array – compact arrangements of seismometers that sample the wavefield at discrete detector sites [4, 5], mathematically resembles that of electronic waves scattering by crystalline atomic sites [6].

The similarities between different fields offer a unified mathematical description, but their differences can be leveraged to improve sampling strategies. Our work is motivated by one such difference: in seismology, seismometers may or may not be arranged periodically, depending on the desired application, while in solid-state crystals, atoms are arranged periodically. However, the discovery of aperiodic but long-range ordered atomic arrangement in solids, known as quasicrystals [7, 8] portrayed that wave propagation in aperiodic media can differ significantly from their periodic counterparts [9].

For example, electronic wave functions scattering from quasicrystalline lattices behave differently from typical metals or insulators, resulting in an unusual electrical-conductance scaling with the system size [8, 10].

Numerous quasicrystals have been either grown or found in nature [11, 12], and quasicrystalline metamaterials that scatter other types of waves, such as light or sound, also show peculiar wave propagation. For example, photonic crystals show a fractal hierarchy of band gaps [13] among other phenomena [14–17], and acoustic metamaterials can reach isotropic effective speeds of sound and isotropic acoustical activity [18]. Characteristic quasicrystalline phenomena and structures can be seen in numerous other platforms, including ultra-cold atomic lattices [19], decorated metallic surfaces [9], polaritonic systems [20] microwave networks [21], acoustic [18] and mechanical [22] metamaterials, botanic [23] and even architecture [24].

In exploration geophysics, randomized or aperiodic acquisition parameters (source and receiver positions and source timing) are used to optimize seismic surveys to reduce the amount of data while recovering dense datasets [25, 26]. Aperiodicity is starting to be considered in seismic cloaking applications [27]. However, the academic seismology community has yet to embrace quasicrystals as a design principle.

The benefit of embracing aperiodicity in seismology lies in that aperiodic sampling patterns can be advantageous in signal processing through signal reconstruction, one of the basis of compressive sensing [28–31]. The Whittaker-Nyquist–Shannon (WNS) sampling theorem [32–34] restricts the faithful reconstruction of a signal from a fi-

* aurmo@geus.dk, corresponding author

† adolfo.grushin@neel.cnrs.fr

nite periodic sampling set. This theorem establishes a bound for the sampling frequency, which must be twice the signal’s maximum frequency to reconstruct it faithfully. The signal reconstruction suffers from aliasing if the sampling happens at a lower frequency than the WNS limit. The WNS sampling theorem applies to periodic sampling, and it was recognized that non-periodic arrays can circumvent its bounds [35]. In particular, quasicrystals provide a stable sampling set [36], defined as one which can reconstruct sparse signals accurately from a set of measurements that are fewer in number than the WNS criterion, even in the presence of perturbative noise. Hence, finding optimal quasicrystals for wave-sampling purposes remains an essential challenge with far-reaching implications in wave physics such as seismology, acoustics, or telecommunication.

Here, we explore a recently discovered family of aperiodic tilings, the Hat family [Fig. 1, 37, 38], to assess its efficiency at beating the WNS sampling limit when sampling spatial seismic wavefields. We show that, among the whole Hat family of tilings, a parameter region around a member of the family, known as the Specter tiling (see Fig. 1), provides ideal properties for unaliased array analysis. For similar inter-station distance, the Specter outperforms all other members of the Hat tiling, as well as other aperiodic tilings such as the famous Penrose tiling [Fig. 1c, 39, 40] or the Square-Triangle tiling [Fig. 1d, 41]. In contrast, other members of the Hat family whose vertices fall closer to periodic tilings, like the Hat tile, perform worse than those with more irregular vertices coordinates. Our results suggest that aperiodic monotiles can have significant applications in array seismology specifically and in the rich variety of fields relying on wavefield sampling beyond.

A. Array Seismology

Historically, array seismology was developed following the United Nations “Conference of Experts to study the methods of detecting violations of a possible agreement on the suspension of nuclear tests” held in 1958 in Geneva [42]. This event sparked numerous efforts to enhance seismic station capabilities globally. Among these initiatives was the introduction of sensor arrays to improve the signal-to-noise ratio of seismic events, an approach borrowed from radio astronomy, radar, acoustics, and sonar. By the 1960s, it had been proven that seismic arrays outperformed traditional single three-component stations in discriminating seismic signals from both earthquakes and explosions [e.g., 43–47].

The deployment of seismic arrays enables the precise detection and analysis of seismic waveforms emanating from various sources, such as tectonic events, volcanic activity, or anthropogenic signals. These arrays, composed of seismometers spatially distributed over a region, allow us to sample the seismic wavefield with a high degree of spatial resolution. The cornerstone of array seismology

lies in its ability to employ data processing techniques, notably *beamforming*, to extract and enhance seismic signals of interest from the background noise. Beamforming methods, in general, rely on a delay-and-sum approach. A signal recorded by the elements of an array will stack coherently when the delays due to the array geometry are adequately taken into account, while the incoherent noise will stack destructively, improving the signal-to-noise ratio (SNR) of the signal of interest [see Methods section, Fig. 8, 4, 5]. This technique is instrumental in understanding the characteristics of the seismic wavefield, facilitating the identification of seismic events, and investigating subsurface structures.

The recent development of inexpensive autonomous and wireless seismic sensors, called nodes, has boosted the deployment of numerous and relatively dense seismic arrays made of hundreds or thousands of instruments [e.g., 48, 49]. These so-called large-N arrays, inherited from industrial hydrocarbon exploration, were initially deployed for seismic *imaging* studies, analyzing seismic waves traveling in the subsurface between sources and receivers to generate numerical images of the structures inside the Earth. Later, they were repurposed as detectors of seismic events, using various beamforming or matched-field processing approaches [e.g., 50, 51]. Often, these arrays are laid out on a regular grid, not optimized for array analysis, and suffer from aliasing problems [50]. On the other hand, arrays designed explicitly for beamforming measurements, such as spiral arrays [52], are not ideal for imaging applications as they produce uneven seismic ray (paths joining sources and receivers) densities beneath the array. Therefore, finding an optimal array geometry that could accommodate beamforming and imaging studies is of great interest to the seismological community.

B. Aperiodic Monotiles

The field of aperiodic tilings, which describes quasiperiodic arrays of vertices of tiles, was recently shaken by the discovery of a new family of tilings: the Hat family [37, 38]. A tiling is a set of tiles that can tessellate the Euclidean plane without gaps or overlaps. A set of tiles may tile the plane periodically, aperiodically, or both. Strong aperiodicity requires that a set of tiles can only tile the plane aperiodically. The problem of finding an aperiodic monotile, i.e., a unique shape that can tile the plane only aperiodically, concluded in March 2023, after more than half a century of search, when [53, 54] proposed the Hat family of tilings (Fig. 1). Unlike other aperiodic tilings, the Hat family of tiles are examples of monotiles that can tile the plane only aperiodically. They improve on the previous record holder, the Penrose tilings [Fig. 1c; 39, 40], that required a minimum of two tiles to tile the plane aperiodically.

The aperiodic tiling family can be constructed from a base, 14-sided polygon whose parallel sides have one of

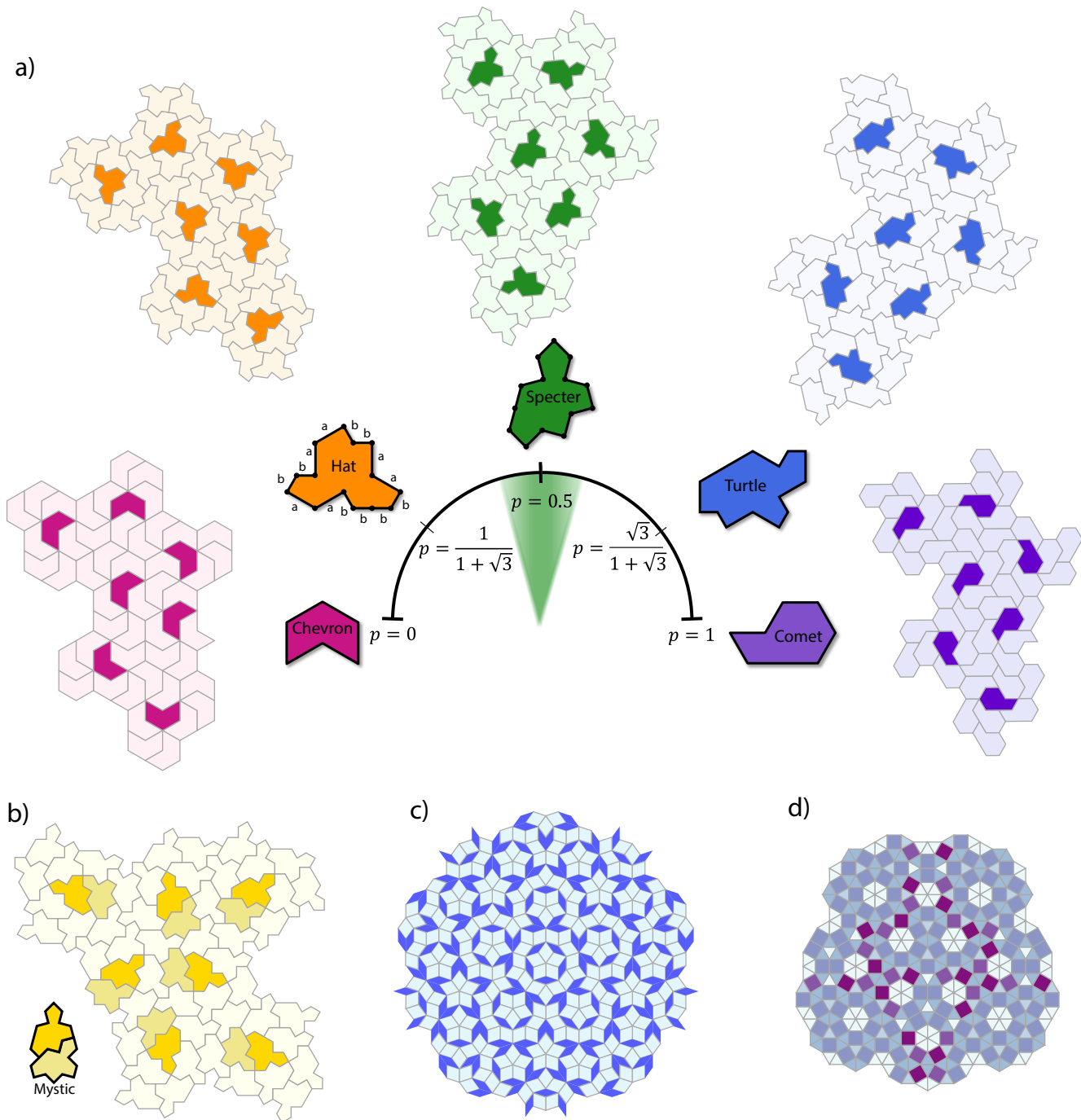


Figure 1. The $\text{Tile}(p)$ family of tilings and other quasicrystals a) We highlight five examples of $\text{Tile}(p)$ tilings, from left to right: $p = 0, \frac{1}{1+\sqrt{3}}, 1/2, \frac{\sqrt{3}}{1+\sqrt{3}}, 1$. These particular tilings are formed by tiles whose names are written on the corresponding tiles. Next to each tile, we show a small portion of the tiling where the mirrored tile needed to generate the tiling is outlined in a darker color. The fourteen vertices of each tile are highlighted by black dots for the Hat and the Specter, and the two length scales, $a = p$ and $b = 1 - p$, are shown around the Hat tile. In the central semicircular diagram, the green shaded area highlights the range of p for which seismic arrays bypass aliasing. b) The Specter tile can also tile the plane aperiodically without using the reflected tile. Instead, it requires the Mystic composite tile, composed of two Specter tiles highlighted with darker colors. c) An example of a Penrose tiling using thick and thin rhombi. d) An example of the aperiodic Square-Triangle tiling.

two lengths, a or b , (see Fig. 1a) The sides can be parameterized by a single parameter $p \in [0, 1]$ with $a = p$ and $b = 1 - p$. The Hat tile amounts to choosing $p = \frac{1}{1+\sqrt{3}}$, while the Specter is the more symmetric choice $p = \frac{1}{2}$ giving an equilateral tile. The Turtle tile is found for $p = \frac{\sqrt{3}}{1+\sqrt{3}}$. The parameter p interpolates continuously between the Chevron ($p = 0$) and the Comet ($p = 1$). These are the two limiting cases that, together with the Specter, can also tile the plane periodically [Fig. 1(a)]. Hereafter, we will refer to the Hat family of tiles as $\text{Tile}(p)$, referring to each tile by its p value. We will use the vertices of single tiles (14 stations) as the basis of single- $\text{Tile}(p)$ MAS arrays. We will refer to the possible tilings by multiple tiles in the family as $\text{Tile}(p)$ tilings, specified by the p value. We will use the vertices of such extended tilings (several hundreds of stations) to define large- N arrays.

Within the Hat family, the Specter tile, or $\text{Tile}(\frac{1}{2})$, is special[55]. While $\text{Tile}(p \neq 0, \frac{1}{2}, 1)$ require both the tile and its mirrored image [Fig. 1a] to tile the plane aperiodically, $\text{Tile}(\frac{1}{2})$ can be made to require only the Specter [38] and not its mirrored image. To achieve this, one forces the use of the Mystic tile (Fig. 1b), which combines two Specters. This means that the tiling with $\text{Tile}(\frac{1}{2})$ has two versions, one without and one with its mirror tile; we call these chiral and achiral $\text{Tile}(\frac{1}{2})$, respectively. Both can tile the plane aperiodically and provide equally good performances at beating aliasing. For completeness, we note that $\text{Tile}(\frac{1}{2})$ can also tile the plane periodically, and therefore it is said to be weakly aperiodic [37], unlike other members of the Hat family. This latter property does not affect any of our results.

Since its discovery, the novel mathematical properties of the Hat tiling ($p = 1/(1 + \sqrt{3})$) have motivated a few novel physical results. When considered as a hypothetical two-dimensional material, the Hat tiling's physical properties lie between those of Graphene and those of aperiodic quasicrystals [17]. The particular connectivity of the Specter tiling allowed the authors of Ref. [56] to find exact solutions for dimer models on this tiling. Other authors have considered the Ising model [57] or the macroscopic elastic behavior of the Hat tiling [58]. However, previous physically motivated research on monotile tilings focused on either the Hat or the Specter tiles. How physical properties change with p remains unexplored.

Each tiling, for any p , can be grown from a single tile by following substitution rules [53, 54]. These rules gather a collection of tiles into metatiles, which are then assembled through matching rules. The procedure can be iterated to create different generations of tilings. The web-app put forward by the discoverers of the Hat family, can be used to visualize this procedure [59]. We append with this work the Python codes that reproduce these tilings, created by adapting the JavaScript code of the cited website into Jupyter Notebooks. See the Data and Code availability section for details on accessing these scripts.

II. BEAMFORMING PROPERTIES OF SINGLE $\text{Tile}(p)$ ARRAYS

We start by describing the properties of seismic arrays made of seismic stations placed at the vertices of a single $\text{Tile}(p)$, leaving the discussion of seismic arrays based on using multiple tiles to Section III.

We will first analyze the beamforming performances of such arrays by computing their corresponding array response function (ARF). The ARF, also known as the structure factor of the lattice, is defined as

$$ARF(\mathbf{k}) = \frac{1}{N^2} \left| \sum_{i=1}^N e^{j\mathbf{x}_i \cdot \mathbf{k}} \right|^2, \quad (1)$$

where N is the number of stations in the array, \mathbf{x}_i their positions, \mathbf{k} is the wavenumber vector and $j^2 = -1$ (see Methods Section for a detailed definition). In crystallography, the ARF of a solid determines its diffraction pattern [6, 8]. Then, we perform synthetic beamforming for different scenarios corresponding to the illumination of the arrays by a single plane wave coming from a single azimuth with a constant velocity or by multiple plane waves covering all azimuths to mimic a homogeneous distribution of seismic noise sources [e.g., 60, 61]. We will compare the robustness against aliasing displayed by $\text{Tile}(p)$ arrays to those of other aperiodic and periodic arrays (see Methods Section and Fig. 9 for a self-contained description of aliasing effects).

A. Array Response Functions of single $\text{Tile}(p)$ arrays

We begin our investigation by analyzing arrays made of a single $\text{Tile}(p)$, i.e., 14 stations (Fig. 1). To compare all arrays on a common scale, we normalize their ARF by the minimum interstation distance r_{min} so that the wavenumber is expressed in terms of multiples of the minimum spatial frequency unit in the array. Effectively, we represent Eq. (1) as a function of a normalized wavevector $\bar{\mathbf{k}} = \frac{r_{min} \cdot \mathbf{k}}{2\pi}$. Figs. 2a, b, and c show the normalized ARFs for the Hat, Specter, and Turtle tiles, respectively. The Hat ARF can be directly compared with the diffraction patterns obtained by [62], who used a much larger set of tiles.

By construction, the vertices of the Hat monotile are a subset of vertices and center points of a hexagonal or equilateral triangular lattice [53], as exemplified by Fig. 2g. Half of the vertices of the Hat share vertices with the triangular lattice (open colored circles in Fig. 2g). Therefore, it is not surprising that the Hat ARF (Fig. 2) bears a strong resemblance with the ARF of a triangular lattice and its sixfold rotational symmetry [63], with the brightest spots of the Hat ARF being at the same positions as the ARF of the triangular tiling. The same

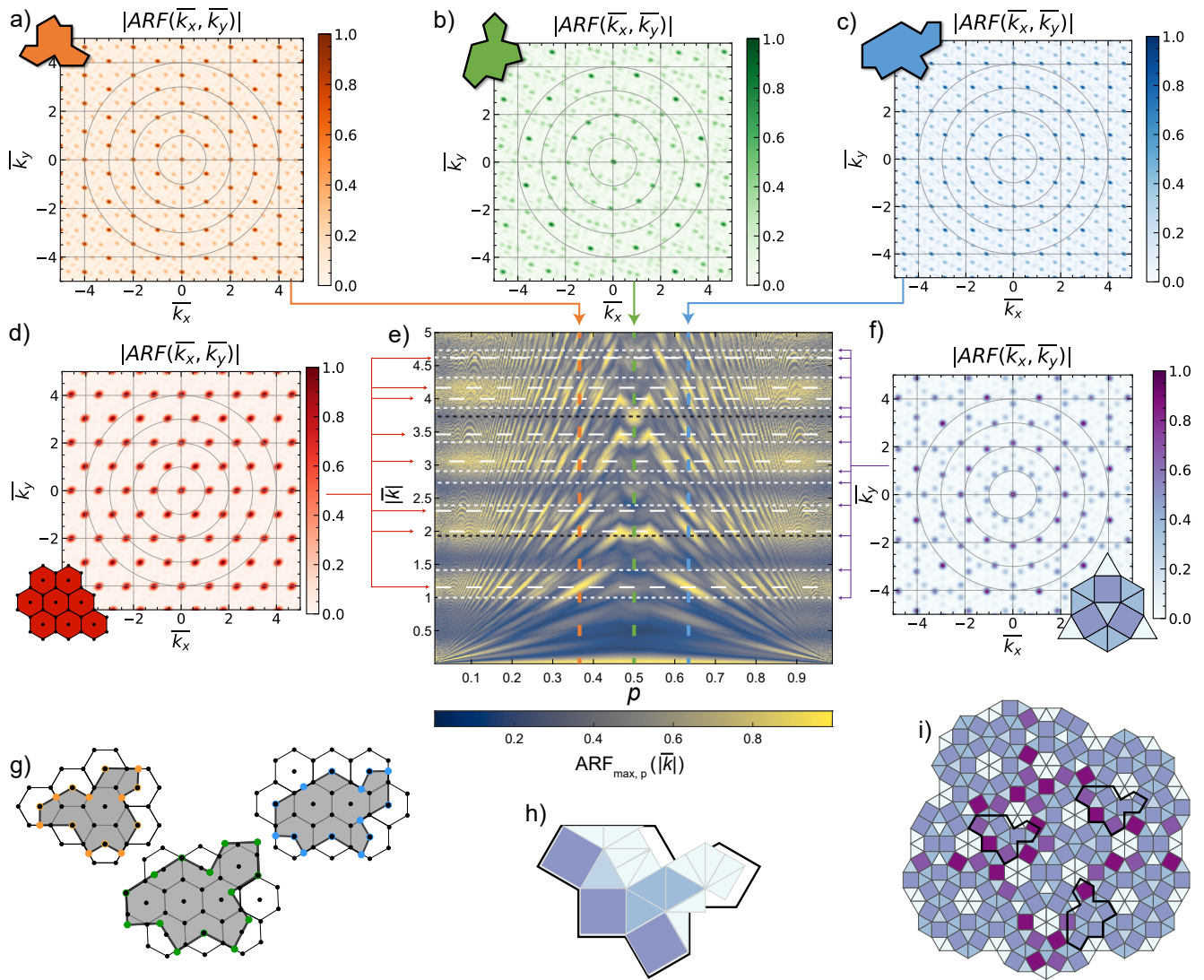


Figure 2. Single Tile(p) ARF analysis. a) ARF of the Hat, b) the Specter, and c) the Turtle as a function of the normalized wavenumber $|\vec{k}|$. d) and f) show the ARF of a Triangular lattice (hexagonal lattice plus its centers) array and the Square-Triangle metatile, respectively. For each p , e) shows the peak sidelobe level as a colormap, calculated using Eq. (2) for each $|\vec{k}|$. The white horizontal dashed lines, indicated by red arrows show the positions of the maxima of the Triangular array ARF (d): $\left[\frac{2n}{\sqrt{3}}, 2n\right]$, $n \in \mathbb{N}$, and their combinations. The white horizontal dotted lines show the maxima of the Square-Triangle metatile ARF (f), indicated by the purple arrows. The black dotted horizontal lines show the positions of the two main sidelobes in common between the Specter and the Square-Triangle ARFs. g) Illustration of the shared vertices between a Triangular lattice and some Tile(p) vertices. The open-colored circles show the shared vertices. The solid circles show the Tile(p) vertices falling outside of the Triangular lattice. h) Re-arrangement of the tiles of the Square-Triangle metatile (g) to form a pseudo-Specter. i) Correspondence between a Square-Triangle aperiodic tiling and the Specter (delineated in black).

observation can be made for the Turtle, albeit with a 30° rotation of the ARF pattern (Fig. 2c).

In contrast, the ARF of the Specter tile (Tile($\frac{1}{2}$), Fig. 2b) exhibits less regularity at small normalized wavenumbers, with no apparent six-fold rotational symmetry and lower amplitude peaks. Despite the angles between consecutive vertices being the same for all Tile(p), they can produce very different ARFs. The Specter's ARF is the only one to exhibit an approximate twelve-

fold rotational symmetry.

Recalling the mathematical similarity between seismic array placements and atomic positions in solids, the Specter's ARF resembles structure factors of aperiodic Square-Triangle tilings [41], which also exhibit a twelve-fold symmetry (see Fig. 2g). These Square-Triangle tilings can be related to several kinds of quasicrystals realized by twisting graphene atomic monolayers [64, 65], or macroscopic spheres arrangements [66]. The similar

symmetry between the Specter’s ARF and the Square-Triangle tiling’s structure factor suggests that the latter lattice can closely approximate the Specter tile. Similar to the Hat and other $\text{Tile}(p)$ sharing a large number of its vertices with a triangular lattice, the Specter shares approximately half of its vertices with the Square-Triangle lattice (Fig. 2i). Another way to illustrate this similarity is by approximating the Specter tile (Fig. 2h) with a rearrangement of the square and triangle metatile shown in (Fig. 2i). The fact that the Specter does not align perfectly with this set of tiles explains the fading of some of the peaks in the ARF compared to the ARF of the Square-Triangle array.

We now wish to assess the performance of $\text{Tile}(p)$ -based arrays regarding aliasing for all p values. Aliasing is mainly controlled by the position of the most prominent amplitude peaks in the ARF, and thus, we need to locate them in the $[\bar{k}_x, \bar{k}_y]$ -space. To do so, we compute the peak sidelobe level $ARF_{max,p}(|\bar{\mathbf{k}}|)$ [67] as the maximum value of each ARF_p along circles of constant $|\bar{\mathbf{k}}|$ values. Mathematically, this operation can be expressed as

$$ARF_{max,p}(|\bar{\mathbf{k}}|) = \max_{\theta \in [0, 2\pi]} ARF_p(|\bar{\mathbf{k}}| \cos \theta, |\bar{\mathbf{k}}| \sin \theta), \quad (2)$$

where $|\bar{\mathbf{k}}| = \sqrt{\bar{k}_x^2 + \bar{k}_y^2}$. Fig. 2e shows $ARF_{max,p}(|\bar{\mathbf{k}}|)$ for $p \in [0, 1]$ and $|\bar{\mathbf{k}}| \leq 5$. We notice several interesting features. First, higher-intensity background horizontal bands can be seen across almost all p . They match the positions of the peaks expected for the triangular lattice, indicated by horizontal dashed lines. Second, this pattern interferes with an M-shape pattern centered at $p = 0.5$. For $p = 0.5$, the maxima as a function of $|\bar{\mathbf{k}}|$ fall on some of the Square-Triangle metatile peaks (black horizontal dotted lines in Fig. 2e). These maxima seem to be unaffected by the triangular lattice background horizontal band modulations.

Moreover, $\text{Tile}(p \in [0.45, 0.55])$ does not have any prominent peaks for $|\bar{\mathbf{k}}| \leq 2$, which suggest an enhanced beamforming performance with respect to aliasing compared to regular arrays. This can be confirmed by noting that the first aliasing peaks of the triangular and square lattice fall at $|\bar{\mathbf{k}}| = \frac{2}{\sqrt{3}} \approx 1.155$ and $|\bar{\mathbf{k}}| = 1$, respectively. Hence, a monotile aperiodic seismic (MAS) array with station positions at the vertices of a single $\text{Tile}(p \in [0.45, 0.55])$ should outperform regular arrays for beamforming analysis with respect to aliasing.

B. Beamforming performances of single $\text{Tile}(p)$ arrays

We now describe synthetic beamforming tests to illustrate the performances of $\text{Tile}(p)$ -based arrays. We use two types of plane-wave source distributions: 1) distributed sources, with a homogeneous azimuthal distribution of 400 sources randomly spanning 360° around

the array. An unaliased beamforming result would show a single high and azimuthally constant intensity ring. 2) a single source coming from -45°N . An unaliased beamforming result would show a single intensity peak. In both cases, we use plane waves with a wavelength equal to twice the smallest inter-station distance in the array (normalized at 1 km) and a slowness of 0.5 s/km, a typical surface wave velocity at 1 Hz. This configuration of minimum inter-station distance and wavelength is at the aliasing limit for a regular square-lattice array, according to the WNS theorem [32–34].

Figure 3 shows the results of this synthetic beamforming for five arrays: a triangular-lattice array (Fig. 3a), the Hat (Fig. 3b), the Specter (Fig. 3c), the Turtle (Fig. 3d), and the Square-Triangle metatile (Fig. 3e). For each array, the second row shows the single source beamforming results while the third row shows the distributed sources beamforming results. In agreement with the ARF analysis, it appears that the Hat and the Turtle arrays (Fig. 3b and d) behave similarly to the triangular array (Fig. 3a) and are strongly aliased. In the single source case, Hat and Turtle arrays exhibit multiple high-intensity peaks having the same amplitude as the main peak (highlighted by the black circle in Fig. 3).

In the distributed sources scenario, we also observe a repetition of the main intensity ring (the “signal” ring, delimited by the black dashed circles in the third row of Fig. 3) across the beamforming diagram. These side-rings are tangent to the signal ring. For regular-lattice arrays, the side rings overlap with each other and with the signal ring (Fig. 3a), and the maxima of the beamforming are not located at the correct slowness values. In a blind beamforming experiment with unknown plane-wave source parameters, extracting meaningful information using the Hat, the Turtle, or the triangular arrays would be challenging because there is no way to identify the main peak (or ring) from its side peaks (or rings) and correctly identify the incoming wave’s slowness.

Notably, the Specter array (Fig. 3c) outperforms the other geometries. In the distributed sources configuration, the Specter array, and to a lesser extent, the Square-Triangle array, presents a well-defined signal ring with minimal side-lobes intensity up to 1.33 s/km. The Specter array shows a homogeneous low-intensity level between 0.5 and 1.33 s/km for the distributed sources, while the Square-Triangle array shows a more pronounced variability. In the single source configuration, the Specter array provides a clear maximum at the expected slowness position of the incoming wave. The side lobes are far from the main peak compared to the Hat, Turtle, and triangular arrays and have smaller amplitudes. The Square-Triangle array has a similar beamforming result, albeit with more numerous and more prominent amplitude side lobes.

To quantify the performances of the $\text{Tile}(p)$ -based arrays, we compute the signal-to-noise ratio (SNR) of the beamforming results for the distributed sources configuration, using the black dashed rings depicted in the third

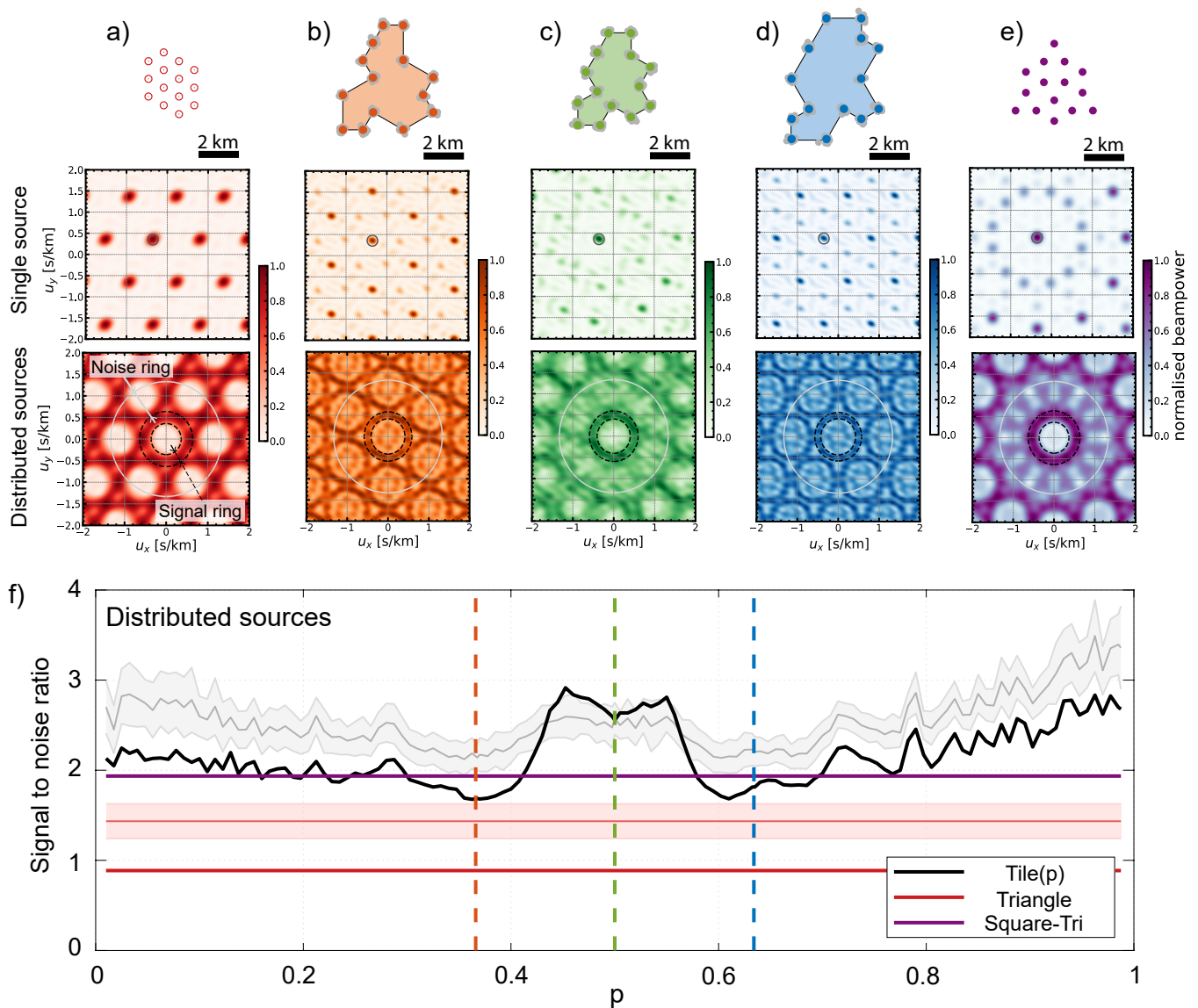


Figure 3. Synthetic beamforming for single $\text{Tile}(p)$ arrays. The first row shows the maps of the arrays. The grey dots for the Hat, Specter, and Turtle tiles are the randomized positions of the stations. The second row shows the beamforming results for a single source coming from the northwest at 2 km/s, highlighted by the black circle. The third row shows the beamforming results for a homogeneous illumination with sources of 2 km/s plane waves distributed around the arrays. The black dashed circles delineate the “signal” ring, and the white circle, the “noise” ring used to compute the signal-to-noise ratio (SNR) in f). The different columns show a) a triangular array, b) the Hat, c) the Specter, d) the Turtle, and e) a Square-Triangle metatile. f) SNR of the beamforming results for the distributed sources as a function of the parameter p . The gray curve and shaded area show the $\text{Tile}(p)$ SNR’s mean and standard deviation, respectively, when perturbing the station positions (gray dots in the first row). Vertical dashed lines highlight the p values of the Hat, Specter, and Turtle arrays. The thick red line shows the SNR for the triangular array. The mean SNR of the triangular array with perturbed positions is shown by the thin red line with the light red shaded area representing the standard deviation. The Square-Triangle array SNR is displayed by the purple horizontal line. The disordered curves are averaged over 100 disorder realizations.

row of Fig. 3. We define the SNR as the ratio of the median amplitude of the inner ring over three times the standard deviation of the amplitude of the outer ring. We chose this definition for the SNR because it gives a value of ≈ 1 for the aliased triangular array. The two rings are

defined by constant-slowness radii. The inner ring (the “signal” ring) is defined between $u_{in,\pm} = u_0 \pm \frac{1}{2f_0 r_{max}}$, and the outer ring (the “noise” ring) is defined between $u_{in,+}$ and $u_{out} = 1.33$ s/km, where $f_0 = 1$ Hz, $u_0 = 0.5$ s/km and r_{max} is the maximum inter-station distance or

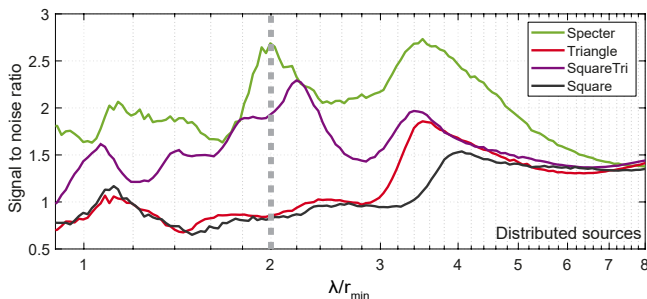


Figure 4. Beamforming SNR as a function of the wavelength. Beamforming SNR for distributed sources as a function of the normalized wavelength for regular square and triangular arrays and for the Specter and Square-Triangle aperiodic arrays. The vertical dashed line indicates the aliasing limit: when the wavelength λ equals twice the minimum interstation distance r_{\min} .

aperture of each array to account for the varying resolution.

The SNR results in Fig. 3f) compares the $\text{Tile}(p)$ in black, the triangular array in red, and the Square-Triangle array in purple. The $\text{Tile}(p)$ family performs at least twice better than regular-lattice arrays and up to three times better in the interval $p \in [0.45, 0.55]$. The Square-Triangle metatile performs on average similarly to the $\text{Tile}(p)$ family but still lies below it on the $p \in [0.45, 0.55]$ range. While not the absolute best in this range, the Specter tile is a good choice as a compromise between performance and design simplicity for a simple 14-station array, beating the aliasing limit of regular-lattice arrays.

We tested the robustness of these results with respect to disordering the position of each station. If a small position error degrades the beamforming performances, then it becomes difficult to envision a field deployment using these geometries. Any obstacle or difficulty in accurately positioning sensors would be detrimental to the quality of the measurements. For each $\text{Tile}(p)$, we varied the position of the 14 sensors randomly drawing from a normal distribution centered on the actual station position and a 100 m variance (10% of the minimum inter-station distance) for a hundred realizations. These positions are displayed as gray points in the array maps of the first row of Fig. 3. The distribution of SNR for each p is shown as the dark gray curve with the gray contour for its mean and standard deviation, respectively. We see that, for $p \notin [0.45, 0.55]$, perturbing the station positions improves the SNR, whereas, for $p \in [0.45, 0.55]$, the SNR is slightly reduced but still exhibits a local maximum. In comparison, perturbing the positions of the triangular array also improves the SNR by about 0.5 but remains below the level of $\text{Tile}(p)$ or Square-Triangle arrays.

The above analysis was calculated at the aliasing limit when the wavelength equals twice the minimum interstation distance in the array. We now explore whether the

Specter array performs better than the other arrays as we vary the wavelength. Figure 4 shows how the beamforming SNR varies when varying the normalized wavelength, $\bar{\lambda} = \lambda/r_{\min}$. The different curves represent the Specter (green), the triangular (red), and the Square-Triangle (purple) arrays, used in Figure 3, and a square-lattice regular array (black). The four arrays exhibit a maximum SNR for $\bar{\lambda} \approx 3.5$. Whether this value is general for most seismic arrays needs further analysis beyond the scope of this paper, but if this is the case, it could serve as a good rule of thumb to optimize seismic array design. Another important observation is the absence of maxima around $\bar{\lambda} \approx 2$ for the regular arrays, consistent with the fact that they suffer from spatial aliasing. In contrast, for the Square-Triangle array and the Specter array, the SNR exhibits a clear maximum at the aliasing limit, and the overall SNR level remains above the level of regular arrays.

This analysis shows that aperiodic tiles possess enhanced beamforming capabilities compared to regular arrays such as square or triangular lattice ones. Among the $\text{Tile}(p)$ family, the window $p \in [0.45, 0.55]$ provides even better results by scattering the intensity of the first side lobes across a wide area and pushing the most energetic side lobes towards larger slowness or wavenumbers. The Specter array, in particular, shows more irregularities in the positions of its ARF side lobes than any other configuration (Fig. 2b). This provides more degrees of freedom to project a wavefield and boosts its beamforming capability. As the building blocks of aperiodic tilings, these tiles and metatiles naturally lack redundancy in their geometry, making them inherently more suitable for beamforming applications than regular lattices.

III. PERFORMANCE OF MULTIPLE $\text{Tile}(p)$ SEISMIC ARRAYS AND COMPARISON WITH OTHER APERIODIC TILINGS

In the previous Section II, we explored the array properties of individual $\text{Tile}(p)$ and compared them with regular or irregular arrays made of a similar number of stations. Here, we explore large-N arrays made of hundreds of stations.

To compare the beamforming capabilities of large-N $\text{Tile}(p)$ -based arrays and other aperiodic tilings, we generate arrays consisting of 310 stations (see Fig. 5). The code accompanying this work can be used to generate seismic arrays of N stations within a geographical region of choice, based on any $\text{Tile}(p)$, Square-Triangle, or Penrose tilings (see Fig. 10 and Methods section).

For the following analysis, we choose a circular region, with an aperture of 2 km, see Fig. 5. On par with single-tile arrays (Fig. 3), we simulate a wavefield generated by either distributed sources or a single source. For each array, we fix the wavelength to be equal to twice the average nearest-neighbor distance (the aliasing limit) and a velocity of 2 km/s.

The results are shown in Fig. 5, one line per array type: Fig. 5a for the triangular array, Fig. 5b for the Specter array, Fig. 5c for the Square-Triangle array and Fig. 5d for the Penrose array. The first column shows the map of each array on the same scale, the second column is the ARF of each array with a logarithmic scale intensity, and the third and fourth columns are the beamforming results for the distributed and single-source scenarios, respectively.

Figs. 5e and f display the SNR of the beamforming as a function of p for the distributed sources and single source configurations, respectively. The horizontal lines in Fig. 5e and f indicate the SNR for the three other geometries: an aperiodic Penrose tiling in blue, an aperiodic Square-Triangle tiling in purple, and a regular triangular lattice array in red. We use the same SNR definition as for the single-tile beamforming (Fig. 3) for the distributed sources scenario. For the single-source scenario, the SNR is defined as the ratio of the maximum intensity within the small black circle (Fig. 5, last column) over the maximum intensity out of the black circle. In this case, $\text{SNR} = 1$ when the signal is aliased.

Overall, we see that aperiodic arrays perform better than regular ones. The SNR profile of large- N $\text{Tile}(p)$ for distributed sources, Fig. 5e, resembles that of single $\text{Tile}(p)$ arrays (Fig. 3f). However, in the present case, the SNR level is more homogeneous across p values except for two evident SNR reductions at both ends of the p spectrum and two dips around the Hat and the Turtle tiles (see orange and blue vertical dashed lines in Fig. 5e). These SNR reductions are again explained by the proximity of these tiles to a regular triangular lattice. In contrast to single tile arrays, we do not observe an SNR maximum for $p \in [0.45, 0.55]$. At this scale, the SNR of the Square-Triangle array is on the same level as the baseline SNR level of the $\text{Tile}(p)$ arrays. The Penrose tiling has an intermediate SNR level between the regular array and the $\text{Tile}(p)$.

The single-source scenario, Fig. 5f, and its specific SNR definition highlight other noteworthy features. First, the SNR is more peaky, and eleven discrete p values produce $\text{Tile}(p)$ arrays that are entirely aliased. Among them, we find the Chevron ($p=0$), the Hat, the Turtle, and the Comet ($p=1$). The number of p values outperforming ($\text{SNR} \geq 2.5$) is also finite, peaking around three p values showing a clearly defined maximum. The Specter is one of them. With this SNR definition, the Penrose and Square-Triangle arrays exhibit better performances than regular arrays, but they are far from the performances of the Specter array. Interestingly, whatever metric we choose to measure the SNR with, all aperiodic tilings outperform compared to the triangular case.

We now analyze the effect of disordering the sensors' positions on the beamforming SNR for distributed sources as a function of the type of tiling. To do so, we randomly perturb the sensor positions, drawing 50 disordered realizations from a normal distribution centered on the actual sensor position with a variable standard

deviation (0% to 35% of the average nearest-neighbor distance).

The results are displayed in Fig. 6a. We see that for all types of arrays, increasing the level of misplacement increases the SNR. This is true up to a plateau where, with more than 30% perturbation, the four types of arrays behave similarly. It is between 10 and 20% of perturbation that the SNR improvement is the strongest. The Specter and Square-Triangle arrays behave similarly despite having different general sensor placements. It is only with more than 15% perturbations that regular arrays reach the same performances as an unperturbed Specter array.

The improvement of SNR with an increased randomization of the station positions can be due to two factors: 1) the overall reduction of the average nearest-neighbor station distance (Fig. 6b) as a function of the randomization level while the wavelength is fixed; 2) a better spatial sampling of the wavefield with fewer redundant elements in the arrays when the randomization is increased, or a combination of both effects. Given the linear trends of the average nearest-neighbor station distance curves (Fig. 6b) and the non-linear increase of SNR (Fig. 6a), we infer that the reduction of the average nearest-neighbor station distance is not the sole responsible for the improvement of the SNR but that the reduction of array redundancies plays a dominant role.

From the average nearest-neighbor station distance, we also see that the Specter and Penrose arrays have a smaller average nearest-neighbor station distance for the same spatial support and number of stations. This means that for a given wavelength, we expect these two geometries to perform better with respect to aliasing as $\bar{\lambda}$ is increased. However, as discussed in the next section, this is not necessarily the case for the Penrose tiling, whose side lobes are controlled by its interstation distance and azimuth distribution (see Discussion section).

IV. DISCUSSIONS AND CONCLUSION

We have explored a newly discovered Hat family of monotile aperiodic tilings [53, 54] from the viewpoint of (seismic) array analysis. The comparison with other well-known aperiodic tilings, such as the Penrose and Square-Triangle tilings, shows that the $\text{Tile}(p)$ tiling could be an ideal geometry for some range of p values. MAS arrays made of one $\text{Tile}(p)$, i.e., 14 stations, exhibit enhanced beamforming performances with larger SNR values for $p \in [0.45, 0.55]$ (Fig. 3) for configurations with distributed sources around the array. For MAS arrays made of hundreds of stations, most of the p spectrum produces large SNRs except for a few notable exceptions: the extreme p values and the Hat and the Turtle (Fig. 5e). If, on top of these results, we add the more restrictive definition of SNR used in the single source configuration (Fig. 5f), then the ranges of p values outperforming in beamforming analysis restrict to $p \in [0.41, 0.43] \cup [0.495, 0.505] \cup [0.57, 0.59]$. For these

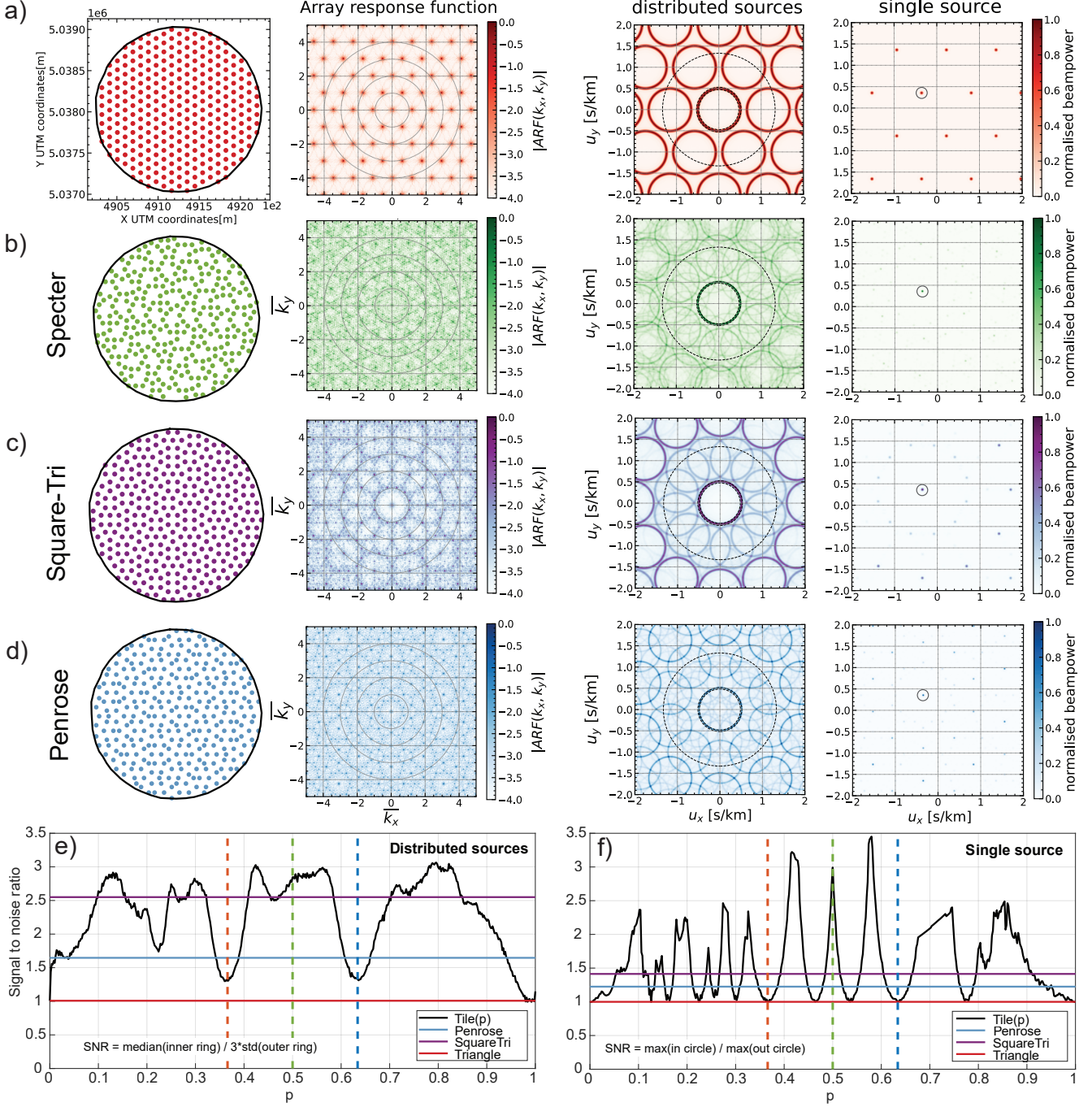


Figure 5. Beamforming performances of Large-N aperiodic arrays. a) from left to right: Station map of the triangular array, ARF (intensity in log scale), beamforming for distributed sources, beamforming for a single source. The rest of the columns show the same as in a) for the b) Specter array, c) the Square-Triangle array, and d) the Penrose array. The black circles in the distributed sources beamforming panels (third column) delineate the areas used to compute the SNR. The black circle in the single source beamforming panels delineates the areas used to compute the SNR. e) SNR of the distributed sources beamforming for the Tile(p) arrays (black curve) as a function of p . The colored horizontal lines show the SNR level for the triangular, the Square-Triangle, and the Penrose arrays. The vertical dashed lines show the p values of the Hat, the Specter, and the Turtle arrays. f) Same as e) for the single source beamforming results. In e) and f) $\text{SNR}=1$ when the signal is aliased and larger if not.

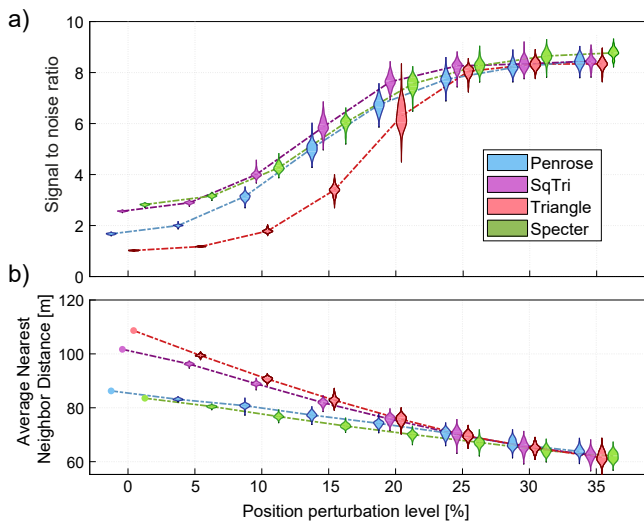


Figure 6. Robustness to sensor misplacement. a) Analysis of the influence of random sensor misplacement on the beamforming SNR of four types of arrays, as a function of the level of randomness (in percent of the average nearest-neighbor station distance in the unperturbed arrays). The beamforming is computed at the aliasing limit of the unperturbed arrays. b) Evolution of the average nearest-neighbor station distance as a function of the position perturbation level. All points are calculated averaging over 50 disorder realizations.

ranges, the side lobes’ amplitude is more than 2.5 times smaller than the amplitude of the main lobe, which effectively mitigates aliasing problems.

An important transversal question for all our analyses is how to compare each geometry fairly. For the single-tile analysis (Fig. 2), we displayed the ARFs normalized by the smallest inter-station distance in the array. This is a standard approach; however, for $\text{Tile}(p \in [0.45, 0.55])$, this minimum distance is not one of the sides of the tile but the distance at the “neck” of the Specter. For this range of p , the minimum distance is unique, representing only about 1% of all possible distances in the array, whereas, for other p -values, the minimum distance is one of the sides and is present multiple times. Therefore, normalizing by the minimum distance might present the Specter and other central- p tiles slightly more favorably than they actually are. On the other hand, this approach allows us to compare all types of arrays consistently; this is why we favored it.

When comparing a single $\text{Tile}(p)$ to other geometries (triangular and Square-Triangle tiling, Fig 3), we had to reach a compromise between the spatial support, the number of stations, and the minimum inter-station distance. It was impossible to set these three parameters equal to the ones of the $\text{Tile}(p)$ simultaneously. The same principle applies to the comparisons in the large- N array cases. We chose to fix the number of stations and the spatial support rather than fixing the minimum interstation distance and varying the number of stations.

It is a scenario closer to the actual seismological practice of array deployment, where we usually have access to a limited number of stations.

Our analysis, spanning several scenarios, while not exhaustive (we, for example, did not test the effect of noisy seismic data, only noisy station positions), is comprehensive enough to demonstrate that Specter arrays (and two other geometries that we conjecture to be around $p = \sqrt{2} - 1 \approx 0.42$ and $p = 2 - \sqrt{2} \approx 0.58$) perform better than regular arrays and some aperiodic ones in general.

The aperiodic nature of the Specter tiling is not the fundamental reason it performs so well: The Hat and Turtle tilings are clear counterexamples of aperiodic tiling suffering from the same aliasing limits as regular arrays. Nor is its monotile nature: the Square-Triangle tiling, made with two tiles, performs almost as well as the Specter tiling. The Specter monotile and large- N arrays made of it are ideal geometries for beamforming applications because they sample azimuths and distances more evenly than any other tested geometry. This is illustrated in Fig. 7a-b, where we can see that the distribution of interstation azimuths is almost uniform for the Specter array.

In contrast, other geometries have oversampled and undersampled azimuthal directions. This is particularly evident for the regular array. The interstation distance distribution is much smoother for the Specter array than for the other arrays. We confirmed these observations quantitatively by computing the normalized entropy of each distribution (Fig. 7c-d), which estimates the distance of a distribution from a pure uniform distribution:

$$\bar{E} = - \frac{\sum_{i=1}^n p_i \log 2(p_i)}{\log 2(n)}, \quad (3)$$

where p_i is the normalized histogram count of the observable, here either the interstation azimuth or the interstation distance, in the bin i and $n = 361$ is the number of bins. Normalized entropy values closer to 1 indicate proximity to a uniform distribution. Again, we observe that most $\text{Tile}(p)$ exhibit a large entropy, except for a few p values, which means that in general, $\text{Tile}(p)$ provides a very uniform distribution of interstation azimuths and distances (Fig. 7c-d). This uniform azimuthal and distance sampling provides the largest number of degrees of freedom possible to sample a wavefield, equivalent to having a coarray (see Methods) that has its sites as homogeneously distributed as possible.

Achieving a homogeneous distribution of points is also possible by drawing coordinates from a uniform distribution. However, homogeneity is guaranteed only on average. In realistic scenarios, only a single realization will be deployed, which is not guaranteed to have uniform azimuthal and distance sampling. In contrast, the homogeneity of the $\text{Tile}(p)$ family is not an average property, and thus, wave sampling will be reproducible and deterministic in practice, unlike placing stations at random.

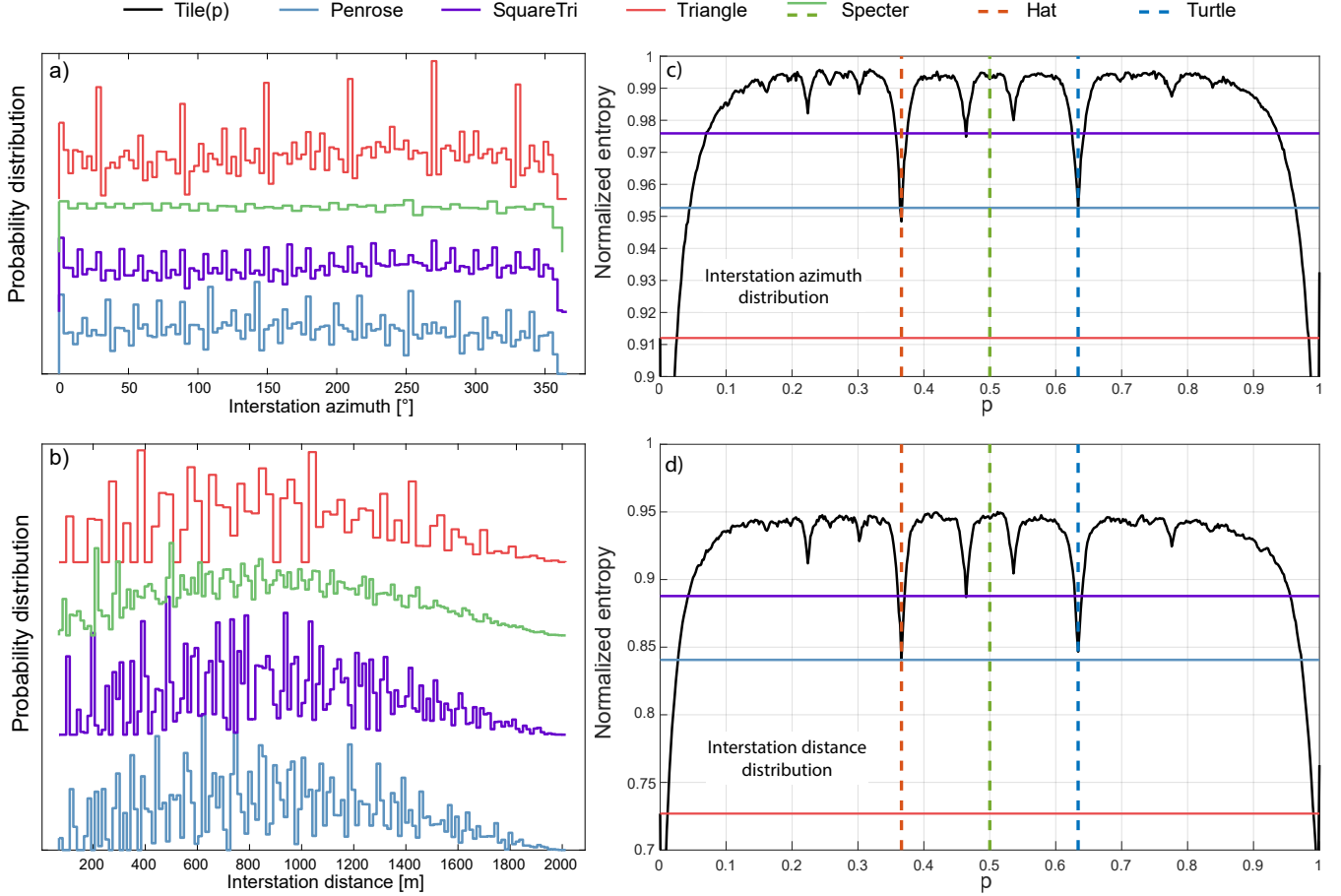


Figure 7. $\text{Tile}(p)$ interstation azimuth and distance distributions entropy. Distributions of interstation azimuths (a) and distances (b) for the four 310-station arrays used in Section III. The normalized entropy (see Eq. (3)) of each distribution is shown by the horizontal lines in c) and d) as well as the normalized entropy of 310-stations $\text{Tile}(p)$ arrays with the black curves. The Specter array has the most homogeneous distributions, with a normalized entropy closest to 1.

Beyond beamforming applications, the ability to homogeneously sample space can be precious for seismic imaging applications, particularly ambient seismic noise tomography using large- N arrays [e.g., 48, 49, 61, 68, 69]. In this technique, homogenizing the rays' azimuthal distribution will produce velocity models where anomalies retain their shape and are less likely smeared by the array imprint, improving their resolution and fidelity. Historically, researchers have used specific and different array designs for beamforming and imaging. Spiral arrays are ideal for beamforming due to their optimal distance and azimuth sampling [52, 70]. However, the ray coverage they produce is not well suited for imaging. On the contrary, dense arrays designed for imaging are often regular [e.g., 61, 71] and may suffer from aliasing when the wavelength becomes smaller than twice the average nearest-neighbor interstation distance. From this point of view, MAS Specter arrays are more versatile and optimal for beamforming and imaging applications altogether.

Our results can also be tested in settings beyond seis-

mology, in physical realizations where the ARF or structure factor can be measured directly. One of these platforms is 3D-printed or nano-patterned disorder photonic crystals. In this context, exploring the Hat family as a design principle for photonic applications, such as band-gap optimization or cloaking [72] is worth exploring. Similar arguments apply to other metamaterial platforms, such as acoustic arrays [73, 74]. Another platform properties where our results can be tested are molecular patterns of the surface of a metal like copper using carbon dioxide molecules [75]. This platform has already been used to design Penrose tilings, where the structure factor was directly measured [9]. Thus, it is a promising system to realize the $\text{Tile}(p)$ tiling and test our findings. Similarly, ultra-cold atomic platforms [76] realizing the Hat tiling could benefit from the results presented here. For example, particle propagation can show characteristic phenomenology in aperiodic lattices [19].

Lastly, as discussed in the introduction, beamforming analysis is strongly tied to the diffraction pattern anal-

ysis of quasicrystals. In this regard, the quasi 12-fold symmetry of the Specter tiling stands out, as it should be explored further to determine the relationship, if any, with other 12-fold symmetry aperiodic tilings, such as the Square-Triangle tiling. Although these further analyses are beyond the scope of this study, we are confident that research on the Hat family of tiling, particularly the Specter tiling, is only in its infancy and will flourish soon. We suggest exploring fields and problems where alignments of points or structures, or lack thereof, are essential, as there is strong potential for practical applications in diverse areas. Besides those mentioned above, we can include wind-farm optimization design or seismic cloaking to cite a few examples.

In conclusion, our work proposes an advantageous design principle based on the recently discovered aperiodic monotiles for seismic arrays to beat the Whittaker-Nyquist-Shannon (WSN) aliasing limit. Monotile aperiodic seismic (MAS) arrays outperform regular and other quasicrystalline arrays in signal-to-noise ratio for single and distributed source scenarios and demonstrate robustness to station position noise, providing a reliable solution in seismic array design. The array-response-function and beamforming analysis we presented here can be directly applied, without any conceptual modification, to rationalize generic wave scattering off aperiodic monotile sites. Hence, the benefits of MAS arrays can be directly exported to numerous other fields, e.g., the placement and design of telecommunications antennae, ad-atoms in solid-state physics, and compressed sensing of various digital signals.

ACKNOWLEDGMENTS

We thank P. Roux and L. Seydoux for discussing and suggesting randomizing the station positions. We are also grateful to C. de France for the hospitality and G. Hendrick for discussions while starting this project. We thank F. Flicker, S. Franca, H. Roche, M. Yoshii, and J. Schirrmann for discussions and related collaborations. A. G. G. acknowledges support from the European Research Council (ERC) Consolidator grant under grant agreement No. 101042707 (TOPOMORPH). A. M. acknowledges support from the Agence Nationale pour la Recherche (ANR) through the project ANR-22-CE49-0019 (MACIV).

DATA AND CODE AVAILABILITY

The Python Jupyter Notebooks used to produce the tiling data and figures will be made available after peer review on the GEUS Dataverse. They are attached as a .zip file for the review process.

AUTHORS CONTRIBUTIONS

Conceptualization: Aurelien Mordret and Adolfo G. Grushin; methodology: Aurelien Mordret; software: Aurelien Mordret and Adolfo G. Grushin; validation: Aurelien Mordret and Adolfo G. Grushin; formal analysis: Aurelien Mordret and Adolfo G. Grushin; writing original draft, review, and editing: Aurelien Mordret and Adolfo G. Grushin;

Appendix A: Plane-wave beamforming

Plane-wave beamforming is used to determine the unknown slowness parameters of waves recorded by a seismic array. The principle of plane-wave beamforming is illustrated in Figure 8. The signal data recorded by the array are shifted in time according to trial slowness vector parameters and then stacked. The maximum intensity of the stacked signals is displayed on a matrix at the position of the trial slowness vector. A grid search is performed over each pixel of the beamforming diagram. The beamforming diagram exhibits a maximum intensity for a slowness vector matching the true slowness of the plane wave recorded by the array.

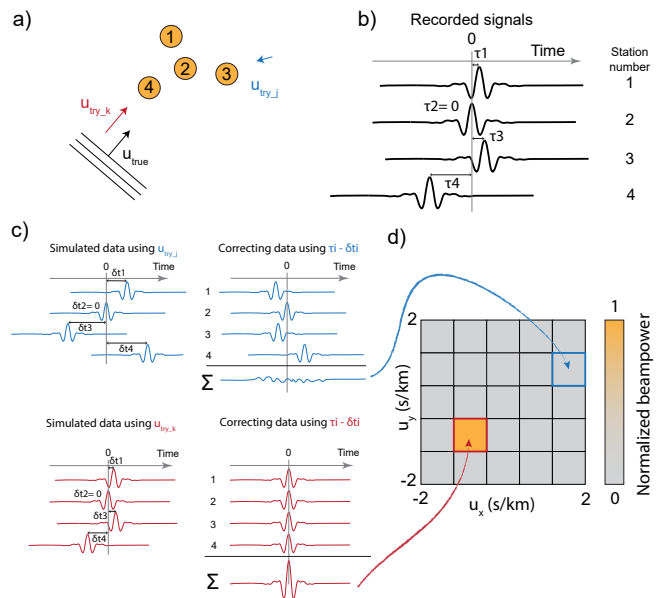


Figure 8. Beamforming principle. a) Map of the seismic arrays. The arrows show the (unknown) true slowness vector of the incoming plane wave (black) and two trial slowness vectors in red and blue. b) The signal recorded by the four seismic stations, with station 2 as the reference station. c) Correction of delays and sum of the signals according to the trial slowness vectors. d) The intensities of the stacked signals are displayed on the beamforming diagram at the positions of the trial slowness vectors (one per pixel). The intensity is maximum for a slowness trial vector close to the true slowness vector.

Mathematically, beamforming can be expressed as follows. We will describe an array of N stations that record a seismic signal $\mathbf{s}(\mathbf{x}_i, t) = \mathbf{s}_i(t)$, where $i = [1, \dots, N]$ is the station index, $\mathbf{x}_i = [x_x, x_y, x_z]$ the geographical coordinates of the station i with respect to the centroid x_0 of the array, and t is the time. We are interested in planar arrays, so we assume $\mathbf{x}_i = [x_x, x_y]$. A plane-wave $v(\mathbf{k}_0) = e^{j\mathbf{k}_0 \cdot \mathbf{x}}$, with $j = \sqrt{-1}$, traveling across the array with a wavenumber vector $\mathbf{k}_0 = [k_x, k_y, k_z]$, will arrive at each station with a time-delay $\tau_i = \mathbf{x}_i \cdot \mathbf{k}_0 = \mathbf{x}_i \cdot (\omega \cdot \mathbf{u}_0)$. Here, $\omega = 2\pi f$ is the angular frequency, f is the frequency, and \mathbf{u}_0 is the slowness vector, i.e., the inverse of the plane-wave velocity. The array-stacked signal, the sum of all signals, is maximum when all the traces from each station are in phase. This happens when the time-delay τ_i is adequately corrected for at each station before summation, i.e., when the wavenumber used to compute the time-delay is equal to the actual wavenumber of the incoming plane wave.

The beampower or beamforming intensity (abbreviated to beamforming in this work) $B(\mathbf{k}, \omega)$, i.e., the intensity of the array-stacked signal, computed for trial plane-waves with wave vectors \mathbf{k} and at frequency ω is [5]

$$B(\mathbf{k}, \omega) = \frac{1}{N^2} \left| \sum_{i=1}^N s_i(\omega) e^{j\mathbf{x}_i \cdot \mathbf{k}} \right|^2. \quad (\text{A1})$$

In Eq. (A1), $s_i(\omega)$ is the temporal Fourier transform of $s_i(t)$ defined by

$$s_i(\omega) = \int_{-\infty}^{\infty} s_i(t) e^{j\omega t} dt. \quad (\text{A2})$$

For horizontally propagating waves, the wave vector simplifies to $\mathbf{k} = [k_x, k_y] = \omega \cdot \mathbf{u}$, where $\mathbf{u} = [u_x, u_y]$ is the horizontal slowness vector. The beamforming is maximized for wavenumbers corresponding to actual plane waves crossing the array from the right azimuths with the right slowness.

Alternatively, the beamforming can be written as

$$\begin{aligned} B(\mathbf{k}, \omega) &= \frac{1}{N^2} \left(\sum_{i=1}^N s_i(\omega) e^{j\mathbf{x}_i \cdot \mathbf{k}} \right)^* \times \left(\sum_{l=1}^N s_l(\omega) e^{j\mathbf{x}_l \cdot \mathbf{k}} \right), \\ &= \frac{1}{N^2} \left(\sum_{i=1}^N \sum_{l=1}^N e^{-j\mathbf{x}_i \cdot \mathbf{k}} \mathbf{C}_{il}(\omega) e^{j\mathbf{x}_l \cdot \mathbf{k}} \right), \\ &= \frac{1}{N^2} \left(\sum_{i=1}^N \sum_{l=1}^N \mathbf{C}_{il}(\omega) e^{j\mathbf{r}_{il} \cdot \mathbf{k}} \right), \end{aligned} \quad (\text{A3})$$

where $\mathbf{C}_{il} = s_i(\omega)^* s_l(\omega)$ is the covariance matrix of the data [e.g., 77], $\mathbf{r}_{il} = \mathbf{x}_l - \mathbf{x}_i$ is the inter-station distance between sensors i and l , and $*$ is the complex conjugate [5]. Therefore, plane-wave beamforming can be seen either as the projection of the physical array data onto

plane waves (Eq. (A1)) or the projection of the physical array data cross-correlations (Eq. (A3)), i.e., the virtual data from a virtual array made of N^2 stations located at coordinates \mathbf{r}_{il} , projected onto plane-waves. This virtual array is called the *difference coarray* [67, 78], or simply *coarray* in this work, and has been introduced in array seismology by [79]. The coarray is the spatial auto-correlation of the physical array coordinates and is defined as the set \mathbb{A} :

$$\mathbb{A} = \{\mathbf{y} | \mathbf{y} = x_2 - x_1, \forall x_1, x_2 \in \mathbf{X}\}, \quad (\text{A4})$$

where \mathbf{X} is the set of coordinates of the physical array. In mathematical morphology [80], the coarray is equivalent to the dilation of \mathbf{X} by itself. The number of unique locations in the coarray and the homogeneity of their spatial distribution determine the array's resolution and anti-aliasing capabilities.

1. Array response function

The array response function (ARF) is usually defined as the beamforming for a plane-wave illuminating all the stations of the array at the same time from below, i.e., a plane-wave with an infinite velocity or a wavenumber $\mathbf{k} = 0$. From Equation (A1), the ARF simplifies as

$$\text{ARF}(\mathbf{k}, \omega) = \frac{1}{N^2} \left| \sum_{i=1}^N e^{j\mathbf{x}_i \cdot \mathbf{k}} \right|^2. \quad (\text{A5})$$

Similarly, Equation (A3) gives

$$\text{ARF}(\mathbf{k}, \omega) = \frac{1}{N^2} \left(\sum_{i=1}^N \sum_{l=1}^N e^{j(\mathbf{x}_l - \mathbf{x}_i) \cdot \mathbf{k}} \right), \quad (\text{A6})$$

which has the same support as the spatial Fourier transform of the coarray. Both the ARF and the coarray encapsulate the geometrical features of the physical array and its capabilities in terms of resolution and robustness to aliasing effects. In the $[k_x, k_y]$ plane, the ARF exhibits a central lobe at $k_x = k_y = 0$ and several side-lobes more or less far from the main lobe with positions and amplitudes depending on the array geometry. In solid-state physics, the ARF is called the structure factor, and it is defined by the atomic positions and measured by X-ray scattering. [e.g., 81].

2. Resolution and aliasing

The resolution of an array is determined by its aperture, i.e., the largest interstation distance within the array, $r_{max} = \max\{\mathbf{r}\}$, and can be measured from the width of the main central lobe of the ARF. The resolution

assesses how well a given array can distinguish two plane waves with similar slowness. A standard approximation of the slowness resolution is $u_R = 1/(2fr_{max})$, using the frequency f . Inversely, aliasing is controlled by the smallest interstation distance in the array, $r_{min} = \min\{\mathbf{r}\}$, and is manifested by the repetition of the ARF pattern at larger wavenumber or slowness, according to the WNS theorem. Based on regular array approximation, the distance in slowness at which the pattern repeats is given by $u_{WNS} = 1/(2fr_{min})$. The ideal array design will aim at narrowing the main lobe while reducing the amplitudes of the side lobes and pushing them towards higher slowness.

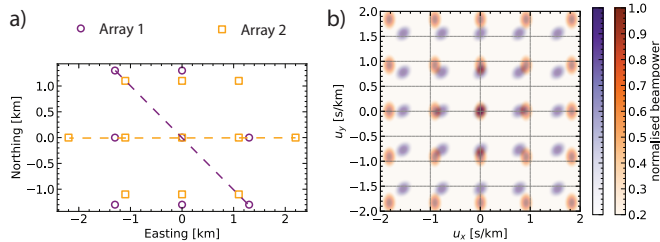


Figure 9. Resolution and aliasing illustration for two regular arrays. a) Map of the two arrays. The dashed lines show the two arrays’ maximum inter-station distances or apertures. b) Superposition of the ARFs of the two arrays, in purple for Array 1 and in orange for Array 2.

Fig. 9 illustrates the effect of the array design on resolution and aliasing. Array 1 (purple circles in Fig. 9a) comprises eight stations located on a 1.1 km square lattice with an aperture of 3.11 km. Array 2 (orange squares in Fig. 9a) comprises eleven stations assembled on a 1.3 km square lattice with a 5.2 km aperture. The corresponding apertures are indicated by dashed lines in Fig. 9 a. Fig. 9b shows the ARF for both arrays. We can see how the lobes of Array 2 are narrower thanks to the larger aperture and are pushed away to higher slowness thanks to the smaller interstation distances. Note that the lobes for both arrays are elliptical because the two arrays are elongated in the North-West and East-West directions for Array 1 and 2, respectively.

Appendix B: Building $\text{Tile}(p)$ arrays of N stations

In this section, we will show how to design large arrays made of multiple $\text{Tile}(p)$ given a user-defined number of stations and a predefined spatial support. We include a suite of Jupyter Notebooks (see Data and Code availability section) to generate such arrays. There are four Notebooks available for four different tilings: Achiral $\text{Tile}(p)$ (Fig. 1a), Chiral Specter (Fig. 1b), Square-Triangle (Fig. 1d), and Penrose-rhombic aperiodic tilings (Fig. 1c). The Penrose and Square-Triangle tiling generators are Python translations from Matlab codes by Eddins [82] and Ho [83], respectively. The $\text{Tile}(p)$ and

Chiral Specter tilings are translated from Kaplan [59]. The remaining Notebooks in the supplementary package reproduce relevant parts of the figures displayed in this paper.

The first step to generating a seismic array is to define its spatial support. Here, we use Google Earth Pro [84] to create a *polygon* encompassing the area where one wants to install the seismic array (black contour in Fig. 10), and we save it as a KML file. The code reads the coordinates of the polygon in the Universal Transverse Mercator (UTM) format and requires that the polygon be defined on a unique UTM zone. The second step is to define the number of stations N (plus or minus a small range δN , to allow the algorithm to converge more easily) that one wants to fit within the polygon. The third step is generating a large enough tiling with more (unique) vertices than the user-predefined number of stations (orange dots in Fig. 10). The algorithm will then scale the vertices iteratively with a user-defined scaling factor until $N \pm \delta N$ vertices fit within the polygon (purple dots in Fig 10). The selected vertices coordinates are then saved in a KML file. Fig. 10 shows an example of designing a 499 stations array located in the French Massif Central within a circular domain based on an achiral Specter tiling.

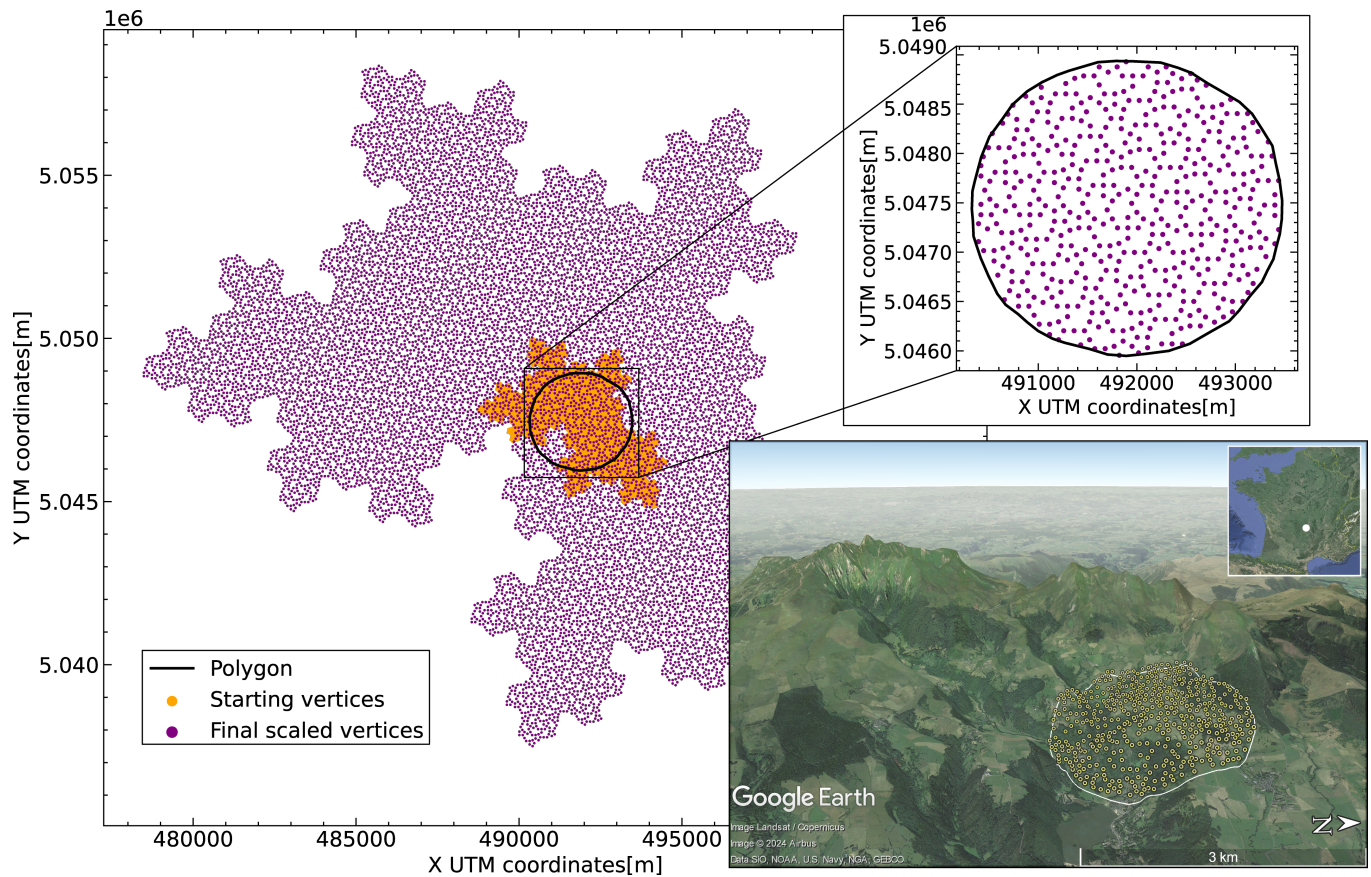


Figure 10. Deployment simulation of Large- N Tile(p) MAS array. Generating a 499-station achiral Specter array within a circular area located in the French Massif Central. The Google Earth inset shows the location of the array wrapped on an exaggerated topography ($\times 2.5$).

-
- [1] M. Costa, A. L. Goldberger, and C.-K. Peng, Multiscale entropy analysis of biological signals, *Physical Review E—Statistical, Nonlinear, and Soft Matter Physics* **71**, 021906 (2005).
- [2] A. P. Sarvazyan, O. V. Rudenko, S. D. Swanson, J. B. Fowlkes, and S. Y. Emelianov, Shear wave elasticity imaging: a new ultrasonic technology of medical diagnostics, *Ultrasound in medicine & biology* **24**, 1419 (1998).
- [3] J. Morlet, Sampling theory and wave propagation, *Issues in acoustic Signal—image processing and recognition*, 233 (1983).
- [4] S. Rost and C. Thomas, Array seismology: Methods and applications, *Reviews of geophysics* **40**, 2 (2002).
- [5] M. Gal and A. M. Reading, *Seismic ambient noise* (Cambridge Univ. Press, 2019) Chap. Beamforming and polarisation analysis, pp. 32–72.
- [6] N. W. Ashcroft and N. D. Mermin, *Solid State Physics* (Holt-Saunders, 1976).
- [7] D. Shechtman, I. Blech, D. Gratias, and J. W. Cahn, Metallic Phase with Long-Range Orientational Order and No Translational Symmetry, *Phys. Rev. Lett.* **53**, 1951 (1984).
- [8] T. Janssen, G. Chapuis, and M. d. Boissieu, Aperiodic crystals from modulated phases to quasicrystals, *Acta Crystallographica Section A* **74**, 10.1107/s2053273318012032 (2018).
- [9] L. C. Collins, T. G. Witte, R. Silverman, D. B. Green, and K. K. Gomes, Imaging quasiperiodic electronic states in a synthetic Penrose tiling, *Nature Communications* **8**, 15961 (2017), 1707.06554.
- [10] Z. Stadnik, Physical properties of quasicrystals, *Springer Series in Solid-State Sciences* 10.1007/978-3-642-58434-3 (1999).
- [11] G. Y. Onoda, P. J. Steinhardt, D. P. DiVincenzo, and J. E. Socolar, Growing perfect quasicrystals, *Physical review letters* **60**, 2653 (1988).
- [12] L. Bindi, P. J. Steinhardt, N. Yao, and P. J. Lu, Natural quasicrystals, *science* **324**, 1306 (2009).
- [13] M. A. Bandres, M. C. Rechtsman, and M. Segev, Topological photonic quasicrystals: Fractal topological spectrum and protected transport, *Phys. Rev. X* **6**, 011016 (2016).
- [14] M. Notomi, H. Suzuki, T. Tamamura, and K. Edagawa, Lasing action due to the two-dimensional quasiperiodicity of photonic quasicrystals with a Penrose lattice, *Phys. Rev. Lett.* **92**, 123906 (2004).

- [15] L. Levi, M. Rechtsman, B. Freedman, T. Schwartz, O. Manela, and M. Segev, Disorder-Enhanced Transport in Photonic Quasicrystals, *Science* **332**, 1541 (2011).
- [16] Y. E. Kraus, Y. Lahini, Z. Ringel, M. Verbin, and O. Zeitlinger, Topological States and Adiabatic Pumping in Quasicrystals, *Phys. Rev. Lett.* **109**, 106402 (2012).
- [17] J. Schirmann, S. Franca, F. Flicker, and A. G. Grushin, Physical properties of an aperiodic monotile with graphene-like features, chirality, and zero modes, *Phys. Rev. Lett.* **132**, 086402 (2024).
- [18] Y. Chen, M. Kadic, S. Guenneau, and M. Wegener, Isotropic chiral acoustic phonons in 3D quasicrystalline metamaterials, *Phys. Rev. Lett.* **124**, 235502 (2020).
- [19] M. Sbroscia, K. Viebahn, E. Carter, J.-C. Yu, A. Gaunt, and U. Schneider, Observing Localization in a 2D Quasicrystalline Optical Lattice, *Physical Review Letters* **125**, 200604 (2020), 2001.10912.
- [20] D. Tanese, E. Gurevich, F. Baboux, T. Jacqmin, A. Lemaître, E. Galopin, I. Sagnes, A. Amo, J. Bloch, and E. Akkermans, Fractal energy spectrum of a polariton gas in a Fibonacci quasiperiodic potential, *Phys. Rev. Lett.* **112**, 146404 (2014).
- [21] P. Vignolo, M. Bellec, J. Böhm, A. Camara, J.-M. Gaubaud, U. Kuhl, and F. Mortessagne, Energy landscape in a Penrose tiling, *Phys. Rev. B* **93**, 075141 (2016).
- [22] Y. Wang and O. Sigmund, Quasiperiodic mechanical metamaterials with extreme isotropic stiffness, *Extreme Mechanics Letters* **34**, 100596 (2020).
- [23] N. Rivier, A botanical quasicrystal, *Le Journal de Physique Colloques* **47**, C3 (1986).
- [24] P. J. Lu and P. J. Steinhardt, Decagonal and quasicrystalline tilings in medieval islamic architecture, *science* **315**, 1106 (2007).
- [25] G. Hennenfent and F. J. Herrmann, Simply denoise: Wavefield reconstruction via jittered undersampling, *Geophysics* **73**, V19 (2008).
- [26] F. J. Herrmann, Randomized sampling and sparsity: Getting more information from fewer samples, *Geophysics* **75**, WB173 (2010).
- [27] S. R. Kumawat, S. Pujari, M. Kumar, and A. Laskar, Numerical study on one-dimensional aperiodic foundations for seismic isolation of structures, in *Symposium in Earthquake Engineering* (Springer, 2022) pp. 283–293.
- [28] D. L. Donoho, Compressed sensing, *IEEE Transactions on information theory* **52**, 1289 (2006).
- [29] C. Mosher, S. Kaplan, and F. Janiszewski, Non-uniform optimal sampling for seismic survey design, 74th EAGE Conference and Exhibition incorporating EUROPEC 2012 , cp (2012).
- [30] F. B. da Silva, R. von Borries, and C. J. Miosso, Golden number sampling applied to compressive sensing, 2018 IEEE Southwest Symposium on Image Analysis and Interpretation (SSIAI) , 1 (2018).
- [31] C. Tsingas, W. Jeong, M. Almubarak, and Y. Ma, Compressive sensing principles applied for seismic data acquisition and processing in time and space, 84th EAGE Annual Conference & Exhibition **2023**, 1 (2023).
- [32] E. T. Whittaker, Xviii.—on the functions which are represented by the expansions of the interpolation-theory, *Proceedings of the Royal Society of Edinburgh* **35**, 181–194 (1915).
- [33] H. Nyquist, Certain topics in telegraph transmission theory, *Transactions of the American Institute of Electrical Engineers* **47**, 617 (1928).
- [34] C. Shannon, Communication in the presence of noise, *Proceedings of the IRE* **37**, 10 (1949).
- [35] E. J. Candès and M. B. Wakin, An introduction to compressive sampling, *IEEE signal processing magazine* **25**, 21 (2008).
- [36] B. Matei and Y. Meyer, Simple quasicrystals are sets of stable sampling, *Complex Variables and Elliptic Equations* **55**, 947 (2010), <https://doi.org/10.1080/17476930903394689>.
- [37] D. Smith, J. S. Myers, C. S. Kaplan, and C. Goodman-Strauss, An aperiodic monotile, *Preprint at https://arxiv.org/abs/2303.10798* (2023).
- [38] D. Smith, J. S. Myers, C. S. Kaplan, and C. Goodman-Strauss, A chiral aperiodic monotile, *Preprint at https://arxiv.org/abs/2305.17743* (2023).
- [39] R. Penrose, The role of aesthetics in pure and applied mathematical research, *Bull. Inst. Math. Appl.* **10**, 266 (1974).
- [40] R. Penrose, Pentaplexity a class of non-periodic tilings of the plane, *The mathematical intelligencer* **2**, 32 (1979).
- [41] M. Oxborrow and C. L. Henley, Random square-triangle tilings: A model for twelffold-symmetric quasicrystals, *Physical Review B* **48**, 6966 (1993).
- [42] UN-Secretary-General, Report of the conference of experts to study the possibility of detecting violations of a possible agreement on the suspension of nuclear tests: note by the secretary-general, *United Nations* (1958).
- [43] E. Carpenter, An historical review of seismometer array development, *Proceedings of the IEEE* **53**, 1816 (1965).
- [44] E. Carpenter, Explosion seismology: Capabilities and limitations of long-range methods for detecting and recognizing explosions are discussed., *Science* **147**, 363 (1965).
- [45] P. E. Green, R. Frosch, and C. Romney, Principles of an experimental large aperture seismic array (lasa), *Proceedings of the IEEE* **53**, 1821 (1965).
- [46] J. Capon, R. Greenfield, R. Kolker, and R. Lacoss, Short-period signal processing results for the large aperture seismic array, *Geophysics* **33**, 452 (1968).
- [47] J. Capon, R. J. Greenfield, and R. T. Lacoss, Long-period signal processing results for the large aperture seismic array, *Geophysics* **34**, 305 (1969).
- [48] F.-C. Lin, D. Li, R. W. Clayton, and D. Hollis, High-resolution 3d shallow crustal structure in long beach, california: Application of ambient noise tomography on a dense seismic array, *Geophysics* **78**, Q45 (2013).
- [49] A. Mordret, P. Roux, P. Boué, and Y. Ben-Zion, Shallow three-dimensional structure of the san jacinto fault zone revealed from ambient noise imaging with a dense seismic array, *Geophysical Journal International* **216**, 896 (2019).
- [50] C. Gradon, L. Moreau, P. Roux, and Y. Ben-Zion, Analysis of surface and seismic sources in dense array data with match field processing and markov chain monte carlo sampling, *Geophysical Journal International* **218**, 1044 (2019).
- [51] J. C. Castellanos, R. W. Clayton, and A. Juarez, Using a time-based subarray method to extract and invert noise-derived body waves at long beach, california, *Journal of Geophysical Research: Solid Earth* **125**, e2019JB018855 (2020).
- [52] B. L. N. Kennett, J. Stipcevic, and A. Gorbatov, Spiral-Arm Seismic Arrays, *Bulletin of the Seismological Society of America* **105**, 2109 (2015).

- [53] D. Smith, J. S. Myers, C. S. Kaplan, and C. Goodman-Strauss, An aperiodic monotile, arXiv preprint arXiv:2303.10798 (2023).
- [54] D. Smith, J. S. Myers, C. S. Kaplan, and C. Goodman-Strauss, A chiral aperiodic monotile, arXiv preprint arXiv:2305.17743 (2023).
- [55] Since we are not interested in strong aperiodicity in this work we use the names $\text{Tile}(\frac{1}{2})$ and Specter interchangeably. In [38], the Specter has wiggled edges deformed from $\text{Tile}(\frac{1}{2})$ to enforce strong aperiodicity. For beamforming purposes, only the inter-site distances and relative angles matter. Hence, the $\text{Tile}(\frac{1}{2})$ and Specter have the same beamforming properties.
- [56] S. Singh and F. Flicker, Exact solution to the quantum and classical dimer models on the spectre aperiodic monotiling, *Phys. Rev. B* **109**, L220303 (2024).
- [57] Y. Okabe, K. Niizeki, and Y. Araki, Ising model on the aperiodic smith hat, *Journal of Physics A: Mathematical and Theoretical* **57**, 125004 (2024).
- [58] R. Rieger and A. Danescu, Macroscopic elasticity of the hat aperiodic tiling, *Mechanics of Materials* **193**, 104988 (2024).
- [59] C. Kaplan, *An aperiodic monotile* (2023).
- [60] N. Harmon, C. Rychert, and P. Gerstoft, Distribution of noise sources for seismic interferometry, *Geophysical Journal International* **183**, 1470 (2010).
- [61] A. Mordret, M. Landès, N. Shapiro, S. Singh, P. Roux, and O. Barkved, Near-surface study at the valhall oil field from ambient noise surface wave tomography, *Geophysical Journal International* **193**, 1627 (2013).
- [62] C. S. Kaplan, M. O’Keeffe, and M. M. Treacy, Periodic diffraction from an aperiodic monohedral tiling, *Acta Crystallographica Section A: Foundations and Advances* **80** (2024).
- [63] J. E. S. Socolar, Quasicrystalline structure of the hat monotile tilings, *Phys. Rev. B* **108**, 224109 (2023).
- [64] S. J. Ahn, P. Moon, T.-H. Kim, H.-W. Kim, H.-C. Shin, E. H. Kim, H. W. Cha, S.-J. Kahng, P. Kim, M. Koshino, et al., Dirac electrons in a dodecagonal graphene quasicrystal, *Science* **361**, 782 (2018).
- [65] W. Yao, E. Wang, C. Bao, Y. Zhang, K. Zhang, K. Bao, C. K. Chan, C. Chen, J. Avila, M. C. Asensio, et al., Quasicrystalline 30 twisted bilayer graphene as an incommensurate superlattice with strong interlayer coupling, *Proceedings of the National Academy of Sciences* **115**, 6928 (2018).
- [66] E. Fayen, L. Filion, G. Foffi, and F. Smalenburg, Quasicrystal of binary hard spheres on a plane stabilized by configurational entropy, *Physical Review Letters* **132**, 048202 (2024).
- [67] J.-F. Hopperstad and S. Holm, The coarray of sparse arrays with minimum sidelobe level, *Proc. IEEE Nordic Signal Processing Symposium (NORSIG 1998)*, 137 (1998).
- [68] M. Chmiel, A. Mordret, P. Boué, F. Brenguier, T. Lecocq, R. Courbis, D. Hollis, X. Campman, R. Romijn, and W. Van der Veen, Ambient noise multimode rayleigh and love wave tomography to determine the shear velocity structure above the groningen gas field, *Geophysical Journal International* **218**, 1781 (2019).
- [69] C. Tsarsitalidou, G. Hillers, B. Giammarinaro, P. Boué, L. Stehly, and M. Campillo, Long Period Rayleigh Wave Focal Spot Imaging Applied to USArray Data, *Journal of Geophysical Research: Solid Earth* **129**, e2023JB027417 (2024).
- [70] Y. Sheng, A. Mordret, F. Brenguier, L. Tomasetto, Q. Higuieret, C. Aubert, D. Hollis, F. Vernon, and Y. Ben-Zion, Tracking Seismic Velocity Perturbations at Ridgecrest Using Ballistic Correlation Functions, *Seismological Research Letters* **10.1785/0220230348** (2024), <https://pubs.geoscienceworld.org/ssa/srl/article-pdf/doi/10.1785/0220230348/6313533/srl-2023348.1.pdf>.
- [71] Y. Sheng, A. Mordret, K. Sager, F. Brenguier, P. Boué, B. Rousset, F. Vernon, Q. Higuieret, and Y. Ben-zion, Monitoring seismic velocity changes across the san jacinto fault using train-generated seismic tremors, *Geophysical Research Letters* **49** (2022).
- [72] K. Vynck, R. Pierrat, R. Carminati, L. S. Froufe-Pérez, F. Scheffold, R. Sapienza, S. Vignolini, and J. J. Sáenz, Light in correlated disordered media, *Reviews of Modern Physics* **95**, 045003 (2023), 2106.13892.
- [73] E. Chéron, J.-P. Groby, V. Pagneux, S. Félix, and V. Romero-García, Experimental characterization of rigid-scatterer hyperuniform distributions for audible acoustics, *Phys. Rev. B* **106**, 064206 (2022).
- [74] K. Tang, Y. Wang, S. Wang, D. Gao, H. Li, X. Liang, P. Sebbah, Y. Li, J. Zhang, and J. Shi, Hyperuniform disordered parametric loudspeaker array, *Phys. Rev. Appl.* **19**, 054035 (2023).
- [75] K. K. Gomes, W. Mar, W. Ko, F. Guinea, and H. C. Manoharan, Designer Dirac fermions and topological phases in molecular graphene, *Nature* **483**, 306 (2012), 10.1038/nature10941.
- [76] I. Bloch, J. Dalibard, and W. Zwerger, Many-body physics with ultracold gases, *Rev. Mod. Phys.* **80**, 885 (2008).
- [77] L. Seydoux, N. M. Shapiro, J. de Rosny, F. Brenguier, and M. Landès, Detecting seismic activity with a covariance matrix analysis of data recorded on seismic arrays, *Geophysical Journal International* **204**, 1430 (2016).
- [78] R. T. Hoctor and S. A. Kassam, The unifying role of the coarray in aperture synthesis for coherent and incoherent imaging, *Proceedings of the IEEE* **78**, 735 (1990).
- [79] R. A. Haubrich, Array design, *Bulletin of the Seismological Society of America* **58**, 977 (1968).
- [80] J. Serra, Mathematical morphology, in *Encyclopedia of Mathematical Geosciences* (Springer, 2022) pp. 1–16.
- [81] D. Levine and P. J. Steinhardt, Quasicrystals: A new class of ordered structures, *Phys. Rev. Lett.* **53**, 2477 (1984).
- [82] S. Eddins, *Penrose rhombus tiling* (2024), gitHub repository. Retrieved April 19, 2024.
- [83] I.-L. Ho, *Generate periodic-to-quasiperiodic unit blocks to fill space* (2024), MATLAB Central File Exchange. Retrieved April 19, 2024.
- [84] Google Earth Pro, Polygon, Retrieved April 18, 2024, from <http://earth.google.com/> (2024), google Earth version 9.3.1.